Short-Arc Correlation and Initial Orbit Determination For Space-Based Observations

Kohei Fujimoto and Daniel J. Scheeres
The University of Colorado at Boulder

CONFERENCE PAPER

Situational awareness of Earth-orbiting particles such as active satellites and space debris is highly important for all current and future space-faring nations. Previous research has proposed a correlation and initial orbit determination technique for ground based optical observations where multiple admissible region maps are intersected in the orbit element space. In this paper, a new application of the admissible region to space-based observations is introduced. A modification must be made to the correlation process as the observer's state is always a valid solution. Numerical examples for several observation scenarios performed well, including LEO-on-GEO and GEO-on-GEO observations.

1. INTRODUCTION

Situational awareness of Earth-orbiting particles such as active satellites and space debris is highly important for future human activities in space. Currently, objects in MEO and GEO are mostly observed by ground-based optical sensors which can detect objects on the order of 10^1 centimeters in diameter at these altitudes [1]. Space-based observations allow for tracking of smaller objects, and several missions have been flown to this date [2]. In 1997, the Space Based Visible (SBV) sensor on the Midcourse Space Experiment (MSX) satellite became a contributing sensor to the Space Surveillance Network (SSN) after the completion of its primary mission for the Ballistic Missile Defense Organization [3, 4]. The Space Based Surveillance System (SBSS) launched in 2010 is a follow-up satellite to MSX/SBV dedicated to the task of space situational awareness (SSA) [5]. The European Space Agency (ESA) as well as the Japanese Ministry of Defense have also shown interest in space-based SSA [6, 7].

For optical observations of Earth-orbiting objects, either ground- or space-based, only the angles and angular rates of the track can be determined. That is, the range and range-rate remain largely unknown. Therefore, to determine the orbit of the observed object, multiple observations must be combined. It is generally uncertain, however, whether two arbitrary tracks are of the same object. This is the crux of the *too short arc* (TSA) problem [8, 9]. Fujimoto and Scheeres have proposed a correlation technique for ground-based observations which uses an uncertainty region of the range and range-rate of an observed object, or the *admissible region*, defined based on some physical constraints of the possible orbits [10, 11]. The intersection of multiple admissible regions can be used to correlate optical observations as well as give an initial state estimate. Furthermore, the propagation of the admissible region over time can be linearized locally to speed up computation.

In this paper, the admissible region method is applied to space-based optical observations of Earth-orbiting particles. First, the admissible region, as well as other necessary concepts, are introduced and defined mathematically (*Background*). Next, we examine examples of processing simulated optical observations of objects in both MEO and GEO from an observer in either LEO or GEO (*Examples*). For space-based observations, the observer's state is always a correlating solution, albeit degenerate. This issue is addressed by excluding a small region about the observer's state in the admissible region. The LEO observer case works well, but the GEO observer case experiences numerical issues due to lack of relative motion. Therefore, if we are to place an observer close to the GEO region, we recommend a slightly eccentric and inclined orbit ($e \sim 10^{-3}$, $i \sim 10^{-1}°$) and separating the observations by about 10 hours. Finally, the effect of observation error to the admissible region technique is discussed quantitatively (*Errors in the Admissible Region Map*). Errors in the observations as well as any dynamical modeling errors impose a definite upper bound on the accuracy of state estimation. This paper sets the theoretical groundwork for correlating space-based observations and obtaining an initial orbit estimate via the admissible region method.

2. BACKGROUND

In this section, we discuss the necessary concepts required in the paper. First, we define our description of optical observations via the attributable vector and its corresponding admissible region. Next, we explain how we correlate

the observations by means of transformations to a common comparison state space and epoch time. A more detailed discussion on this correlation method can be found in Fujimoto and Scheeres [11].

2.1   Optical Observations and the Attributable Vector

For optical-only observations of Earth-orbiting objects, only the angles and angular rates of the track can be determined [10]. That is, the range and range rate remains largely unconstrained. Thus, each track can be mathematically expressed in terms of an *attributable vector* $\mathcal{A}$ at epoch t of the observation [8, 9]:

$$\mathcal{A} = (\alpha, \delta, \dot{\alpha}, \dot{\delta}) \in [-\pi, \pi) \times (-\pi/2, \pi/2) \times \mathbb{R}^2, \tag{1}$$

where α and δ specify the topocentric angular position of the object. A discussion of how one may estimate an attributable vector from a given track of data can be found in Maruskin, et al [10]. J2000 is chosen as the coordinate system in this paper so that α is the right ascension and δ is the declination, but note that one is free to choose any coordinate system of their choice. For a more complete description of the track, we append the time t_0 of the observation as well as the geocentric position $\mathbf{P_O}$ and velocity $\dot{\mathbf{P}}_O$ of the observation point:

$$\mathfrak{X} = (\mathcal{A}, t_0, \mathbf{P_O}, \dot{\mathbf{P}}_O). \tag{2}$$

In this paper, we assume that we have perfect knowledge regarding the state of the observing satellite. This assumption allows us to use the same formulation of the attributable vector as ground-based observations except for the dynamics of the observation point. Qualitatively, we expect this assumption to be good especially when the observer is in a LEO orbit because the errors in the observer's state (10^1 meter-level in position, 10^0 millimeter/second-level in velocity [2, 12]) is much less than the uncertainty in range / range-rate. A quantitative discussion is in the *Errors in the Admissible Region Map* section.

2.2   The Admissible Region

For any attributable vector $\mathfrak{X}$, we can take different values of range and range-rate ($\rho, \dot{\rho}$) to complete the topocentric spherical coordinates of the particle and thus obtain different physical orbits. However, not all of these orbits are relevant for any given application. For instance, we may not be interested in objects that escape Earth orbit a couple of hours after observation. Rather, a closed region of the ($\rho, \dot{\rho}$) plane can be defined such that all of the physically relevant orbits are contained within the interior of this region. We define this region as the *admissible region* $F_{\mathfrak{X}}$ and each point in the admissible region as *virtual particles* (VP) [9]. A set of criteria $\mathcal{C}$ defining the admissible region for ground-based observations have been proposed by Marsukin, et al [10]. For this paper, we modify the criteria as follows:

$$\mathcal{C} = \bigcap_{i=1}^{4} \mathcal{C}_i, \tag{3}$$

and

$$
\begin{aligned}
\mathcal{C}_1 &= \{(\rho,\dot{\rho}) : E \le 0\} & \mathcal{C}_2 &= \{(\rho,\dot{\rho}) : 0 \le \rho \le 14\} \\
\mathcal{C}_3 &= \{(\rho,\dot{\rho}) : 1.03 \le r_p\} & \mathcal{C}_4 &= \{(\rho,\dot{\rho}) : r_a \le 25\},
\end{aligned}
\tag{4}
$$

where E is the specific geocentric energy of the debris particle, and r_p and r_a are the perigee and apogee radii, respectively. Units of length are in Earth radii (r_E). The main difference is that the range of topocentric range values now includes objects that are very close to the observer. Fig. 1 is an example of an admissible region.

2.3   Object Correlation and Initial Orbit Determination

Suppose we have multiple admissible regions $F_{\mathfrak{X}1}, F_{\mathfrak{X}2}, \ldots, F_{\mathfrak{X}n}$ each based on uncorrelated optical tracks made potentially at different times and observation locations. To determine whether these observations are correlated,
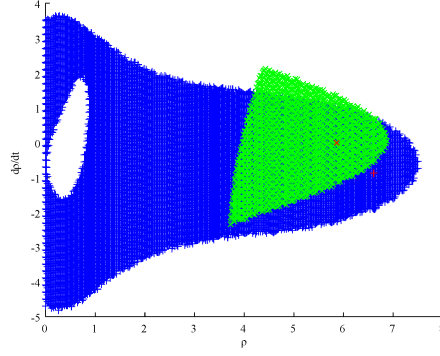
Fig. 1. Admissible regions based on observations of an object in GEO from an observer in LEO
(blue "+") and a ground observation point (green "x").
The red points indicate the true object state for each observation type.

we map their respective admissible regions to a common state space and propagate them to a common epoch time τ with some transformation $T(\tau, t_i)$, where $i = 1, 2, \ldots, n$. In this paper, we use the Poincaré orbit element space as the common space, which are non-singular canonical orbit variables [12, 13]:

$$l = \Omega + \omega + M \qquad\qquad \mathfrak{L} = \sqrt{\mu a}$$

$$\mathfrak{g} = \sqrt{2\mathfrak{L}\left(1 - \sqrt{1 - e^2}\right)}\cos(\omega + \Omega) \qquad \mathfrak{G} = -\mathfrak{g}\tan(\omega + \Omega) \tag{5}$$

$$\mathfrak{h} = \sqrt{2\mathfrak{L}\sqrt{1 - e^2}\,(1 - \cos i)}\cos\Omega \qquad \mathfrak{H} = -\mathfrak{h}\tan\Omega,$$

where a is the semi-major axis, e is the eccentricity, $i \in [0, \pi]$ is the inclination, $\Omega \in [-\pi, \pi]$ is the right ascension of the ascending node, $\omega \in [-\pi, \pi]$ is the argument of periapsis, $M \in [-\pi, \pi]$ is the mean anomaly, and μ is the standard gravitational parameter. We expect that if the observations are related, then their admissible region maps $T(\tau, t_i) \circ F_{\mathfrak{X}i}$ would intersect at the same state space coordinate as the observed object. Furthermore, since T is invertible and continuous, each $T(\tau, t_i) \circ F_{\mathfrak{X}i}$ are 2-dimensional manifolds embedded in 6-dimensional space. From arguments from topology, the probability that any 2 admissible region maps intersect randomly is 0 [14]. Fig. 2 is a graphical representation of this method.
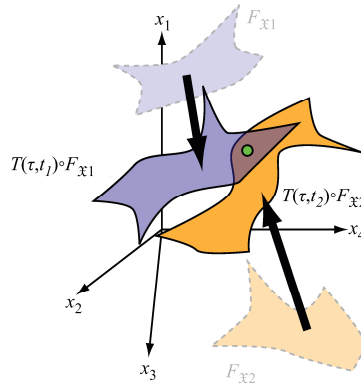

Fig. 2. Map T evolves admissible regions $F_{\mathfrak{X}1}$ [blue] and $F_{\mathfrak{X}2}$ [orange] from two separate observations to a common epoch τ. The intersection point [green] is where the observed object most likely exists in state space.

In order to convert the above theory into a computational algorithm, it is both natural and advantageous to regard each admissible region map $T(\tau, t_i) \circ F_{\mathfrak{X}i}$ as a probability density function (pdf) over the Poincaré space, as each point on the admissible region is a potential estimate of the observed object's state with some assigned probability. We discretize the Poincaré space into many 6-dimensional hypercubes which we refer to as *bins*. Suppose we have

two pdfs *f* and *g* each associated to an admissible region. Then, we can "combine" the information content of these pdfs into a new pdf *h* via Bayes' rule:

$$h = \frac{f \cdot g}{\sum (f \cdot g)},$$
(6)

where the sum is over the span of the discretized Poincaré space. In a graphical sense, pdf *h* is a cut out of the region where *f* and *g* intersect: *h* > 0 for any bins where both *f* > 0 and *g* > 0, and the probability expressed by *h* is one that is evaluated over this overlap region. Again, since two admissible region maps do not intersect randomly in a 6-dimensional space, one can simply look at whether *h* > 0 for some bin to deduce with confidence whether or not the two observations are correlated. Furthermore, the location of bins for which *h* > 0 provide an initial orbit estimate of the observed object. This estimate can be introduced as the reference orbit for a statistical orbit determination method, such as the Kalman filter [15].

By treating the information from the optical observations as pdfs, not only are we able to combine the information from multiple optical tracks, we can also fuse different types of observations as long as they are similarly expressed as pdfs over some state space. For instance, information regarding the spatial distribution of debris can be extracted from a model such as MASTER-2005 so that unrealistic objects are excluded from the admissible region [16].

3. EXAMPLES

In this section, we discuss results of an implementation of the above theory. Our goal is to correlate simulated observations from LEO and GEO of objects in both MEO and GEO. The orbital elements at the epoch time for all observed objects:

> 3 objects in GEO, 1 object in a Molniya orbit, 2 objects in an eccentric MEO orbit,
> 1 object in a circular MEO orbit, 1 object in a GPS orbit

and observing satellites:

> 1 satellite in LEO, 1 satellite in GEO

in this section are listed in Appendix A.

3.1   False Correlation via the Observing Satellite's State

For any attributable vector, the VP corresponding to $(\rho, \dot{\rho}) = (0, 0)$ always maps to the state of the observing satellite. Therefore, if we are to include the origin of the range / range-rate space in the admissible region, then the admissible region maps of any two observations will intersect at this point, leading to false correlations and degenerate orbit solutions. Fig. 3 is an example of one such degenerate case. The overlapping region indeed includes the state of the observing satellite but not any of the observed satellites.
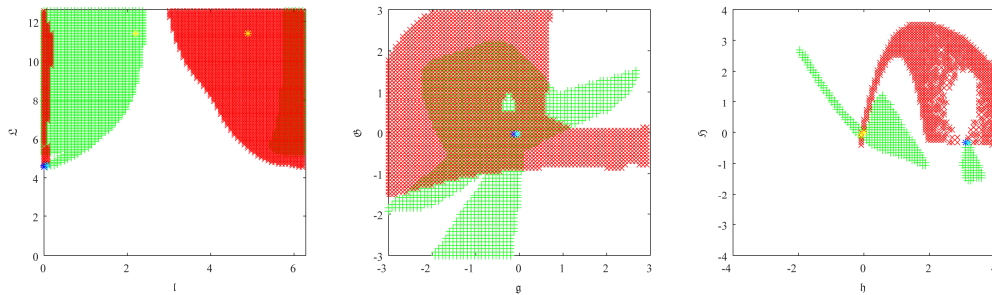

Fig. 3. Projections of admissible region maps when correlating observations from LEO-O of two different objects (GEO1-GEO2). Each subplot is a 2-dimensional subspace of the Poincaré space. The map for GEO1 is in red, GEO2 in green. The blue region is where the two maps intersect. The yellow asterisks indicate the true state of the observed objects, and the cyan asterisk is the state of the observing satellite. Units of length in Earth radii, time in hours, and angle in radians.

We hypothesize that we can remove the observer's solution by reformulating the range criterion for the admissible regions as follows:

$$C_2' = \{(\rho, \dot{\rho}) : \rho_{\mathrm{MIN}} \le \rho \le 14\}, \tag{7}$$

where $\rho_{\mathrm{MIN}} > 0$. $(\rho, \dot{\rho}) = (0, 0)$ is no longer included in the admissible region, so the admissible region maps themselves should not intersect. A false intersection may still be detected by the algorithm, however, depending on the discretization size. Fig. 4 is an illustration of this situation. When the discretization is defined by the bold lines, the algorithm will regard that the two manifolds intersect over the center bin, where as if defined by the dashed lines, the algorithm correctly identifies that the two manifolds do not intersect.
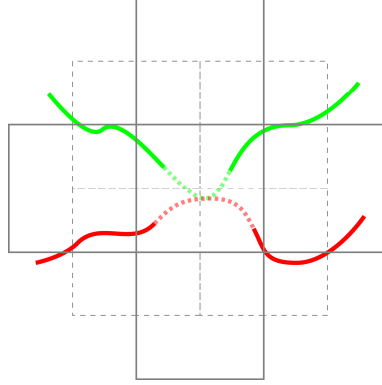

Fig. 4. A schematic showing how a fictitious correlation may occur even when the admissible region has been redefined to exclude the observing satellite's state. The red and green lines represent the two admissible region maps of concern, and the dotted portions are the excluded regions where $0 \le \rho < \rho_{\mathrm{MIN}}$. The gray lines represent bin boundaries.

Thus, it is necessary to refine the discretization over the overlap area of the admissible region maps to correctly test our hypothesis. Bear in mind that the refinement is only valid to the accuracy of the admissible region maps, which is in turn mainly driven by the observation accuracy. In the following examples, we assume zero observation error and apply the refinement technique only to show the validity of the theory in the *Object Correlation and Initial Orbit Determination* section. Refer to the *Errors in the Admissible Region Map* section for a discussion on how errors in the observation and the observer's state affect the admissible region maps.

3.2   Observer at LEO

We now consider correlating a batch of simulated space-based observations with the admissible region method; refer to Fujimoto and Scheeres for pseudo-code [11]. In this example, we simulate 101 error-free observations over 48 hours of the 8 objects in our object set from a near-circular, sun-synchronous orbit at 630 km altitude (LEO-O). Observations are made every 10 minutes, but the same object is not observed twice for at least two hours. Occultation due to the Earth is considered by modeling the Earth and its atmosphere as an opaque sphere of radius 6578 km. We consider the Earth's zonal harmonics up to 5th order and integrate the dynamics numerically using a variable step seventh / eighth-order Runge-Kutta algorithm. The Poincaré space discretization is as follows:

$$\mathbf{X}_{\min} = (4.4621, 0, -3, -3, -4, -4), \mathbf{X}_{\max} = (12.6206, 6.2832, 3, 3, 4, 4)$$
$$\mathbf{M} = (100, 77, 73, 73, 98, 98), \tag{8}$$

where $\mathbf{X}_{\min}$ and $\mathbf{X}_{\max}$ are the bounds of the space and $\mathbf{M}$ is the number of bins in each Poincaré orbit element direction. Consequently, the total number of bins is 3.9408×10^{11}. The bounds were chosen so that all objects in the TLE set were included, and $\mathbf{M}$ was chosen so that the length of the edges of each bin were roughly equal (≈ 0.082). $\rho_{\mathrm{MIN}} = 20$ km and the discretization refinement factor is set to 25. Tab. 1 is a summary of the results. Observations were correctly correlated and the state of all objects were correctly estimated. We conclude that the admissible region method is a viable option for both correlating LEO-based observations and providing an initial orbit estimate.

Tab. 1.The estimation accuracy of each observed object for a LEO observer. "True Sol." and "Degenerate Sol." indicate whether the observed objects state or the observing satellite's state, respectively, is included in the solution.

Object	Number of Obs.	Overlap bins	True Sol.	Degenerate Sol.
GEO1	14	3	YES	NO
GEO2	14	2	YES	NO
GEO3	14	2	YES	NO
MOL1	13	1	YES	NO
EM1	11	1	YES	NO
EM2	13	2	YES	NO
CM1	12	2	YES	NO
GPS1	12	4	YES	NO

3.3 <u>Observer at GEO</u>

When a similar problem as in the previous section is considered for an observer in GEO, the lack of relative motion makes it difficult to remove the degenerate solution. In this example, we simulate 2 error-free observations over 5 hours for each of the 3 GEO objects (GEO1-3) in our object set from a GEO orbit (GEO-O), for a total of 6 observations. Observations are made every 30 minutes, but the same object is not observed twice for at least 4 hours. Occultation due to the Earth, the dynamics of objects, and the discretization of the Poincaré space are the same as the LEO example. ρ_{MIN} = 50 km and the discretization refinement factor is set to 50. Tab. 2 is a summary of the results. Although no false positive correlations are observed, the initial orbit estimates all contain the observing satellite's state. Due to the slow relative motion in GEO, the admissible region maps remain near parallel to each other, and thus a very fine refinement of the state space is required to differentiate the two manifolds near the degenerate solution [11]. Consequently, if we are to process more observations, it is highly likely that they will not be correctly correlated as any admissible region map will intersect at the degenerate solution.

Tab. 2. The estimation accuracy of each observation pair $\{r\}$ for the GEO-O observer.
Δt is the time between observations.

$\{r\}$	Δt	Overlap bins	True Sol.	Degenerate Sol.
GEO1-GEO1	4.0	17	YES	YES
GEO1-GEO2	0.5	0	—	—
GEO2-GEO2	4.0	14	YES	YES
GEO2-GEO3	0.5	0	—	—
GEO3-GEO3	4.0	24	YES	YES

We are able to rectify this situation by adding eccentricity ($e = 0.0001 \rightarrow e = 0.001$) and inclination ($i = 0.0057° \rightarrow i = 0.25°$) to the observer's orbit: we call this new orbit GEO-O'. We also increase the time gap between observations to up to 16 hours to further introduce dynamical change. Tab. 3 shows the improved performance. Note that similarly increasing the observation time gap for the GEO-O observer produced fictitious solutions due to an ambiguity in the number of revolutions the observed object made between observations [11]. As future work, we hope to process a large batch of observations from an observer in or near GEO, much like the LEO observer case.

Tab. 3. The estimation accuracy of each observation pair $\{r\}$ for the GEO-O' observer.

$\{r\}$	Δt	Overlap bins	True Sol.	Degenerate Sol.
GEO1-GEO1	8.0	6	YES	NO
GEO2-GEO2	8.0	3	YES	NO
GEO3-GEO3	16.0	5	YES	NO

4. ERRORS IN THE ADMISSIBLE REGION MAP

In a real-world setting, ambiguity in the observation variables (i.e. angles and angle-rates) as well as the observer's state (i.e. $\mathbf{P}_O$ and $\dot{\mathbf{P}}_O$), which combine to form the attributable vector, give rise to errors in the admissible region map. The errors cause the theoretically 2-dimensional admissible region maps to inflate and become 6-dimensional volumes. Qualitatively, we understand that this inflation is small compared to the planar spread of the maps because

the errors in the attributable vector are "much smaller" than the uncertainties in range and range rate defined by the admissible region: the admissible region can span several Earth radii in range, for example. In addition, the inflation is partially taken into account by discretizing the maps by 6-dimensional hypercubes. In this section, we quantify this argument.

We begin by defining the following static linear transformation from the attributable vector state space (α, δ, $\dot{\alpha}$, $\dot{\delta}$, $\mathbf{P}_O$, $\dot{\mathbf{P}}_O$) to the Poincaré orbit element space at the observation time t_0:

$$\bar{\Phi}(t_0) = \frac{\partial(\mathcal{L}, \mathfrak{l}, \mathfrak{G}, \mathfrak{g}, \mathfrak{H}, \mathfrak{h})^T}{\partial(a, e, i, \Omega, \omega, M)^T}\bigg|_* \cdot \frac{\partial(a, e, i, \Omega, \omega, M)^T}{\partial(x, y, z, \dot{x}, \dot{y}, \dot{z})^T}\bigg|_* \cdot \frac{\partial(x, y, z, \dot{x}, \dot{y}, \dot{z})^T}{\partial(\alpha, \delta, \dot{\alpha}, \dot{\delta}, \mathbf{P}_O, \dot{\mathbf{P}}_O)^T}\bigg|_*, \tag{9}$$

where the asterisk indicates that the partials are evaluated along a reference state. Here, we use the state of the observed object as the reference. The complete linear transform adds a dynamic transform from time t_0 to τ. We consider two-body dynamics with secular J_2 perturbations for this example [17].

We use the following 1-σ values for the attributable vector [2, 10]:

$$\sigma_\alpha = \sigma_\delta = 1.5 \times 10^{-4} \text{ deg} = 2.6180 \times 10^{-6} \text{ rad}$$
$$\sigma_{\dot{\alpha}} = \sigma_{\dot{\delta}} = 1.0 \times 10^{-6} \text{ deg/s} = 6.2832 \times 10^{-5} \text{ rad/hr} \tag{10}$$
$$\sigma_{\mathbf{P}_O} = 10\text{m for LEO, 100 m for GEO in all cartesian directions.}$$

In order to reduce the dimensionality of our analysis, we assume that we have perfect knowledge of the observing satellite's velocity, which usually can be determined to the millimeter/second-level [12].

First, to generate reference orbits, we simulated 126 error-free observations from LEO-O to the objects in our 8 object sample set over the span of 120 hours. The observations were timed according to the rules in the *Observer at LEO* section. Then, deviations in the attributable vector were sampled on the 7-dimensional 3-σ error hyperellipsoid whose bounds are defined above. The maximum absolute Poincaré state deviation, computed with (9), was recorded for each observation. Fig. 5 shows the time evolution of these maxima, and Tab. 4 is a tabulated summary. We find that only the error in $\mathfrak{l}$ grows significantly in time, which is expected as $\mathfrak{l}$ is directly proportional to the mean anomaly. After 120 hours, the state errors are on the same order of magnitude as the discretization for $\mathfrak{l}$, whereas for all other coordinate directions, they remain less than 1/10th of the nominal bin size. This behavior is similar to that of ground-based observations [11].
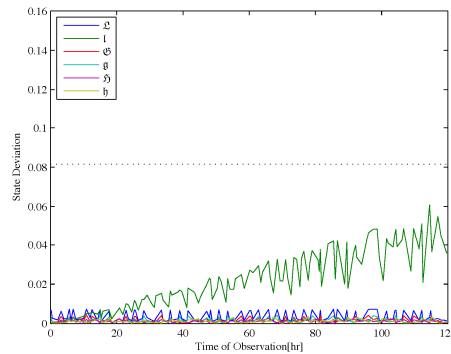

Fig. 5. Errors in the Poincaré orbit elements due to uncertainty in the attributable vector as a function of time for the LEO-O observer. The black dotted line indicates the nominal discretization size.

Tab. 4. The mean and maximum state errors in each Poincaré orbit element direction, as well as the ratio of their values with respect to the nominal discretization size of 0.081586, for the LEO-O observer.

	Mean	(Ratio)	Max	(Ratio)
$\mathfrak{L}$	0.00363	0.04446	0.00731	0.08955
$\mathfrak{l}$	0.02236	0.27401	0.06075	0.74461
$\mathfrak{G}$	0.00169	0.02075	0.00429	0.05261
$\mathfrak{g}$	0.00164	0.02013	0.00416	0.05102
$\mathfrak{H}$	0.00106	0.01299	0.00251	0.03082
$\mathfrak{h}$	0.00117	0.01439	0.00354	0.04335

Fig. 6 and Tab. 5 are results of similar analyses run for the GEO-O observation satellite. Here, the error in $\mathfrak{l}$ grows beyond the nominal discretization size at about 80 hours. This is due to a combination of the larger uncertainty in the observing satellite's state and the higher sensitivity to measurement errors compared to the LEO case. On the other hand, the errors in all of the other coordinate directions are the approximately the same as the previous example.
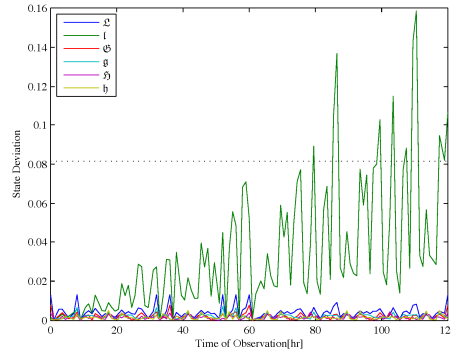

Fig. 6. Errors in the Poincaré orbit elements due to uncertainty in the attributable vector as a function of time for the GEO-O observer. The black dotted line indicates the nominal discretization size.

Tab. 5. The mean and maximum state errors in each Poincaré orbit element direction, as well as the ratio of their values with respect to the nominal discretization size, for the GEO-O observer.

	Mean	(Ratio)	Max	(Ratio)
$\mathfrak{L}$	0.00417	0.05106	0.0131	0.16059
$\mathfrak{l}$	0.03455	0.42342	0.15845	1.94212
$\mathfrak{G}$	0.00221	0.02714	0.00779	0.09553
$\mathfrak{g}$	0.00205	0.02519	0.00705	0.08636
$\mathfrak{H}$	0.00148	0.01818	0.00437	0.05357
$\mathfrak{h}$	0.00154	0.01884	0.0051	0.06251

The errors arising from uncertainty in the attributable vector, along with any dynamical modeling errors, practically limit the state space discretization size. Refining the discretization beyond the level of state error is not recommended; at this point, the information simply does not exist in the observations. Therefore, the discretization refinement employed in the *Examples* section to remove the degenerate solution may not be a realistic option. In such a case, one could either choose a larger value of ρ_{MIN} such that discretization refinement is not necessary, or regard the entire cluster of bins that contains the state of the observer's satellite as degenerate. The above results also suggest that a smarter way to discretize the state space would be to have the least number of bins in the $\mathfrak{l}$-direction, followed by $\mathfrak{L}$ then all other directions.

5. CONCLUSIONS

In this paper, we discussed a new application of the admissible region concept to space-based optical observations of Earth-orbiting objects. The geometry of observations was reformulated such that both the observer and the observed object are influenced by the Earth's gravitational field. When processing simulated space-based observations, the observer's state was always included in the admissible region map, causing all observations to correlate with all other observations. At a theoretical level, this problem can be solved by setting a lower bound on the observation range larger than 0; however, particularly for an observation satellite in GEO, the slow dynamics inhibits the effectiveness of this workaround. If we are to place an observer in a GEO, it should be inclined and eccentric, and the observation gap should be longer than that for a LEO observer. Although perfect knowledge of the observer's state was assumed for the examples in the paper, we gave a quantitative argument on how to assess the errors in the admissible region maps due to observation errors.

As future work, we hope to process a large batch of observations made from a GEO orbit. Alternate efficient methods of removing the degenerate solution may have to be devised for this observation scenario. Furthermore, we would like to add more perturbing forces to our simulation, as well as consider the effects of dynamic modeling errors to the admissible region maps in more detail.

APPENDIX A. ORBITAL ELEMENTS FOR OBJECTS IN THE NUMERICAL EXAMPLE

The classical and Poincaré orbital elements at the epoch time for all 8 observed objects and 2 observer satellites in the Examples section are listed below as

$$(a \ [r_E], e, i \ [\text{rad}], \Omega \ [\text{rad}], \omega \ [\text{rad}], M \ [\text{rad}]), (\mathfrak{L} \ [r_E^2/\text{hour}], \mathfrak{l} \ [\text{rad}], \mathfrak{G} \ [r_E/\text{hour}^{1/2}], \mathfrak{g} \ [r_E/\text{hour}^{1/2}], \mathfrak{H} \ [r_E/\text{hour}^{1/2}], \mathfrak{h} \ [r_E/\text{hour}^{1/2}]),$$

where r_E is Earth radius.

- GEO
[GEO1] (6.6102, 0.0003, 0.0002, 3.1274, 2.3294, 5.7226), (11.4721, 4.8962, 0.0006, 0.0006, −0.0000, −0.0006)
[GEO2] (6.6109, 0.0003, 0.0009, 5.9501, 2.9681, 5.8729), (11.4727, 2.2247, −0.0005, −0.0009, 0.0010, 0.0029)
[GEO3] (6.6109, 0.0001, 0.0001, 3.0902, 4.2464, 6.1176), (11.4727, 0.8879, −0.0003, 0.0001, −0.0000, −0.0002)

- Molniya
[MOL1] (4.1971, 0.7154, 1.1204, 0.8126, 5.1137, 0.1671), (9.1414, 6.0934, 0.8200, 2.1991, −1.9501, 1.8469)

- Eccentric MEO
[EM1] (3.6573, 0.7123, 0.3106, 1.0976, 1.6080, 5.9942), (8.5333, 2.4166, −0.9526, −2.0447−0.6739, 0.3451)
[EM2] (4.1472, 0.5529, 1.2347, 5.5811, 2.4137, 4.8996), (9.0868, 0.3281, −1.7237, −0.2444, 2.0573, 2.4323)

- Circular MEO
[CM1] (3.9994, 0.0006, 1.1284, 4.9148, 4.2128, 2.9461), (8.9234, 5.7905, −0.0005, −0.0017, 3.1297, 0.6421)

- GPS satellite
[GPS1] (4.1645, 0.0048, 0.9599, 2.7242, 3.6934, 2.5851), (9.1057, 2.7195, −0.0019, 0.0143, −1.1296, −2.5474)

- LEO observer
[LEO-O] (1.0988, 0.0001, 1.7088, 1.0000, 0.1000, 0.1000), (4.6772, 1.2000, −0.0002, 0.0001, −2.7450, 1.7625)

- GEO observer
[GEO-O] (6.6109, 0.0001, 0.0001, 1.0000, 0.1000, 0.1000), (11.4727, 1.2000, -0.0003, 0.0002, −0.0003, 0.0002)
[GEO-O'] (6.6109, 0.0010, 0.0044, 1.0000, 0.1000, 0.1000), (11.4727, 1.2000, -0.0030, 0.0015, −0.0124, 0.0080)

REFERENCES

[1]   A. Rossi, "The Earth Orbiting Space Debris," *Serb. Astron. J.*, No. 170, 2005, pp. 1–12.

[2]   D. A. Vallado, "Evaluating Gooding Angles-only Orbit Determination of Space Based Space Surveillance Measurements," 2010. Presented at the *AAS Born Symposium*.

[3]   J. Sharma, G. H. Stokes, C. v. Braun, G. Zollinger, and A. J. Wiseman, "Toward Operational Space-Based Space Surveillance," *Lincoln Laboratory Journal*, Vol. 13, No. 2, 2002, pp. 309–334.

[4]   G. H. Stokes, C. v. Braun, R. Srid haran, D. Harrison, and J. Sharma, "The Space-Based Visible Program," *Lincoln Laboratory Journal*, Vol. 11, No. 2, 1998, pp. 205–238.

[5]   "Space Based Space Surveillance (SBSS) System," memorandum, The Boeing Company. Retrieved from `http://www.boeing.com/` on July 25, 2011.

[6]   T. Flohrer, H. Krag, H. Klinrad, and T. Schildknecht, "Feasibility of performing space surveillance tasks with a proposed space-based optical architecture," *Advances in Space Research*, Vol. 47, 2011, pp. 1029–1042.

[7]   M. Tagawa, T. Hanada, Y. Kitazawa, and A. Kawabe, "Orbital Debris Observation Using Space-based LADAR System," 2011. Presented at the *28th International Symposium on Space Technology and Science*, Okinawa, Japan.

[8]   G. Tommei, A. Milani, and A. Rossi, "Orbit determination of space debris: admissible regions," *Celestial Mechanics and Dynamical Astronomy*, Vol. 97, 2007, pp. 289–304.

[9]   A. Milani, G. Gronchi, M. Vitturi, and Z. Knežević, "Orbit Determination with Very Short Arcs. I Admissible Regions," *Celestial Mechanics and Dynamical Astronomy*, Vol. 90, 2004, pp. 57–85.

[10] J. M. Maruskin, D. J. Scheeres, and K. T. Alfriend, "Correlation of optical observations of objects in earth orbit," Journal of Guidance, Control and Dynamics, Vol. 32, No. 1, 2009, pp. 194–209.

[11] K. Fujimoto and D. J. Scheeres, "Correlation of Optical Observations of Earth-Orbiting Objects and Initial Orbit Determination," 2010. Presented at the *2010 AIAA/AAS Astrodynamics Specialist Conference*, Toronto, Canada. AIAA-2010-7975.

[12] D. Vallado, *Fundamentals of Astrodyamics and Applications*. Hawthorne, CA: Microcosm Press, third ed., 2007.

[13] D. Brouwer, "Solution of the Problem of Artificial Satellite Theory Without Drag," *The Astronomical Journal*, Vol. 64, 1959, pp. 378–396.

[14] J. S. Carter, *How Surfaces Intersect in Space: An introduction to topology*. Singapore: World Scientific, second ed., 1995. pp. 277.

[15] B. D. Tapley, B. E. Schutz, and G. H. Born, *Statistical Orbit Determination*. Burlington, MA: Elsevier Academic Press, 2004. pp. 159-284.

[16] M. Oswald, S. Stabroth, C. Wiedemann, P. Wegener, H. Klinkrad, and P. Vörsmann, "ESA's MASTER 2005 Debris Environment Model," *Advances in the Astronautical Sciences*, Vol. 123, No. 1, 2006, pp. 811–824.

[17] K. Fujimoto, D. J. Scheeres, and K. T. Alfriend, "Analytical Non-Linear Propagation of Uncertainty in the Two-Body Problem," 2011. Presented at the *2011 AAS/AIAA Spaceflight Mechanics Conference*.